PCCP

PAPER

View Article Online
View Journal | View Issue

Cite this: *Phys. Chem. Chem. Phys.*, 2023, **25**, 16294

Synthesis of hierarchical mesoporous cerium titanate brannerite and uranyl adsorption properties at pH 3.8†

Linggen Kong, * Tao Wei, Inna Karatchevtseva and Nicholas Scales

Received 2nd February 2023,
Accepted 5th June 2023

DOI: 10.1039/d3cp00528c

rsc.li/pccp

Cerium titanates possessing brannerite structure are produced by employing soft and hard templates *via* sol–gel processing. Powders synthesized with various hard template sizes and template to brannerite weight ratios are composed of nanoscale 'building blocks' with size ~20–30 nm and characterized on macro-, nano- and atomic scales. These polycrystalline oxide powders exhibit specific surface area up to ~100 $m^2\ g^{-1}$, pore volume ~0.4 $cm^3\ g^{-1}$, and uranyl adsorption capacity ~0.221 mmol (53 mg) U per gram powder. Remarkably, the materials possess significant proportion of mesopores with 5–50 nm pores representing 84–98% of total pore volume, which facilitate fast accessibility of the adsorbate to the internal surfaces of the adsorbent with adsorbed uranyl reaching over 70% of the full capacity within 15 min of contact. These mesoporous cerium titanate brannerites synthesized by the soft chemistry route are highly homogenous, stable at least in 2 mol L^{-1} acidic or basic solution, and may attract attention for other applications like catalysis at high temperature.

1. Introduction

Cerium titanate, possessing a brannerite crystal structure with the synergistic effect of Ce and Ti oxide, has many applications such as photocatalysis,[1–8] electrochemistry,[6,9,10] chemical-mechanical polishing materials,[11,12] and actinide host matrices in nuclear waste forms.[13–15] Recently,[16] $CeTi_2O_6$ brannerite is revealed as the most promising candidate for solar thermochemical hydrogen production due to its essential characteristics including a smaller reduction enthalpy compared to ceria yet large enough to split water, a high thermal stability, and a large entropy of reduction associated with $Ce^{4+} \rightarrow Ce^{3+}$ redox reaction. The conventional synthesis methods, *via* either mixed oxide or soft chemistry route followed by calcination, employ high temperature treatment (1300–1350 °C) to form the brannerite structure.[17–22] The elevated temperature treatment usually leads to the collapse of the pore structure, thus eliminating the porosity features like high specific surface area and pore volume, which are essentially required for most applications. The commonly used sol–gel processing[1–6,23–25] ensures high composition homogeneity of the product due to the chemical reaction at the molecular level, and also likely maintain the porosity features because of the relatively low calcination temperature (500–900 °C).

Various surfactants and/or dispersion agents have been attempted to fabricate porous $CeTi_2O_6$ brannerite. Zhang *et al.*[1–4] have used either a dispersion agent polyethylene glycol (PEG) or a surfactant cetyltrimethyl ammonium bromide (CTAB) *via* sol–gel processing to prepare porous material with major $CeTi_2O_6$ brannerite phase, and minor CeO_2 and rutile TiO_2 phases. The surface area, pore volume and pore size are ~22 $m^2\ g^{-1}$, 0.044 $cm^3\ g^{-1}$ and 36 nm, respectively, at 700 °C heat treatment; and ~16 $m^2\ g^{-1}$, 0.023 $cm^3\ g^{-1}$ and 18 nm after 800 °C calcination, with crystallite sizes ~38.0–42.9 nm. A close examination of the particulate morphology reveals that the final product is composed of agglomerated and/or coalesced nanoparticles. A coprecipitation method has been employed by Ding *et al.*[5] to produce porous crystalline cerium titanate brannerite with ~33.4 $m^2\ g^{-1}$ surface area and 0.13 $cm^3\ g^{-1}$pore volume after 500 °C calcination. However, the crystallinity is very low as shown by XRD pattern. Matějová *et al.*[26] have employed sol–gel processing within reverse micelles followed by calcination at 800 °C to produce $CeTi_2O_6$ brannerite as a single crystalline phase at 7 : 3 Ti : Ce molar ratio with surface area <10 $m^2\ g^{-1}$, which is too low for adsorption application.

Porous metal oxides have been often investigated in nuclear industry applications.[27–34] Besides the requirements for exceptional porosity properties, the physico-chemical durability and the radiolytic stability need to be considered when designing a new adsorbent. Due to the easy control of the porosity and surface functionality, silica is usually studied for radionuclide adsorption. Nevertheless, the complex silicates with a greater

Australian Nuclear Science and Technology Organisation, Lucas Heights, Sydney, New South Wales, Australia. E-mail: linggen.kong@ansto.gov.au

† Electronic supplementary information (ESI) available. See DOI: https://doi.org/10.1039/d3cp00528c

proportion of ⟨Si–O⟩ bond are more susceptible to radiation-induced amorphization[35] and pores are likely to collapse due to irradiation.[36] Alternatively, non-siliceous mesoporous oxides with nanostructure morphology have been investigated extensively,[37–49] and some have been studied for uranium adsorption.[27–34,47–51] In order to increase the sorption capacity or selectivity, binary metal oxide nanoparticles possessing high surface area and/or functionalized groups have been primarily investigated.[52–56] Compared with the binary oxides, the ternary metal oxides may provide increased performance.[33] Nevertheless, the investigation of porous ternary metal oxides is limited, except the zirconium titanium oxides which can reach adsorption capacity for $U \sim 40.5$ mg g^{-1}.[57–62] These mixed metal oxides possess superior characteristics over their single metal oxide counterparts, including improved surface areas and acidities, higher thermal, mechanical, and radiolytic stabilities,[57–61] as well as the enhanced sorption capacity due to the synergistic effect of different metal elements.[62] In addition, the adsorbent matrix could be converted into a highly durable inert ceramic waste form, following saturation with the radioactive species thus providing permanent radionuclide confinement.[63,64] However, the synthesis of fully crystallized metal oxides with a ternary composition and porous morphology structure is rare because low temperature synthesis normally leads to low crystallinity of the materials whereas high temperature treatment results in the loss of the porosity.

In this work, hierarchical mesoporous cerium titanate with brannerite crystal structure is produced by using glucose as a dispersion agent (soft template) and colloidal silica as a hard template. The synthesized powders with different porosities are used to study the uranyl adsorption properties including capacities and kinetics at pH 3.8. Ideally, the overall particle morphologies (size and size range) can be controlled by selection of the dispersion agent and its quantity, while the pore features (specific surface area, pore size and volume) can be tailored by different sizes of the colloidal silica and the silica to brannerite weight ratios. The aim of this work is to synthesize porous brannerite material with minimum secondary phase in presence of colloidal silica, to produce the porous powder with high specific surface area in order to improve adsorption capacity and high proportion of mesopores to promote adsorption rate.

2. Experiments

2.1. Materials

Cerium(III) nitrate hexahydrate (99.9%+) and titanium(IV) (triethanolaminato) isopropoxide [Tyzor TE] (compound dissolved in 2-propanol) were used as-received. Ti content was quantitatively determined by ICP-MS with raw chemical containing 45.84 wt% Tyzor TE. Uranyl stock solution (0.5 mol L^{-1}) was prepared by dissolving U_3O_8 in concentrated nitric acid (69 wt%), evaporating the acid on hotplate and adding water to form pH ~ 4 solution. The exact uranyl [UO_2^{2+}] concentration was measured by ICP-MS. All chemicals, including D-(+)-glucose, were A. R. grade and purchased from Sigma-Aldrich. Milli-Q grade water was used allover experiments. Various types of Ludox® colloidal silica (amorphous silica nanoparticle suspension in water) were purchased from Sigma-Aldrich and used as hard template. Based on the surface area provided by supplier, the average diameter (Φ) of the colloidal silica is calculated assuming the silica nanoparticles are rigid and spherical, and the density of the amorphous silica is 2.196 g cm^{-3}.[65] The surface areas are 320–400, 220, and 135 m^2 g^{-1} for Ludox® SM-30, Ludox® HS-30, and Ludox® AS-40, respectively; the corresponding diameters are 6.8–8.5, 12.4, and 20.3 nm.

2.2. Synthesis procedure

10 mmol $Ce(NO_3)_3{\cdot}6H_2O$ and 22 mmol Tyzor TE were dissolved in 30 mL water to form an aqueous solution. In another container, 3.75 mL concentrated ammonia (25 wt% NH_4OH) was mixed with 16.25 mL water. The ammonia aqueous solution was dropwise added into the above solution while vigorous stirring magnetically, which led to formation of a gel. The final ammonia concentration was ~1 mol L^{-1} with pH = 11.6. The gel was aged for 4 h at 45 °C, forming an oligomer suspension upon stirring. 3.32 g D-(+)-glucose (glucose: metal oxide = 1 : 1 w/w) was added while stirring. Calculated Ludox aqueous suspension was added and subsequently stirred for 1 h to form a homogeneous mixture, which was dried overnight in an oven at 100 °C. The dried gelling material was calcined in a furnace in air at 800 °C (unless otherwise specified) for 6 h with 2 °C min^{-1} ramp rate, and 5 °C min^{-1} cooling rate. The calcined powders were stirred in 2.5 mol L^{-1} NaOH for > 8 h at 40 °C (30 mL of basic solution per 1 g powder) in a polypropylene bottle. This leaching process was repeated three times to remove the silica template. The resultant particulates were washed twice with water to eliminate Na^+, and once with pH 3.8 HNO_3 solution, followed by centrifugation and drying at 100 °C oven overnight.

2.3. Characterization

X-ray diffraction (XRD) analyses were conducted using a PANalytical X'Pert Pro diffractometer with Cu K_α radiation ($\lambda_{\alpha av}$ = 1.541874 Å) at 45 kV and 40 mA. Raman spectra were recorded using a Renishaw inVia Raman spectrometer equipped with the Argon ion laser (532 nm) and a Peltier cooled CCD detector at room temperature. Transmission electron microscopy (TEM) was performed on a JEOL 2200FS instrument, operated at 200 kV, to record selected area electron diffraction patterns (SAED). A Zeiss Ultra Plus Scanning electron microscopy (SEM) operating at 15 kV was used to analyze the microstructures. Surface area, pore volume and pore size were determined using nitrogen sorption analysis at 77 K on Autosorb IQ volumetric adsorption analyzer. Thermo-gravimetric analysis (TGA) was performed using a Netzsch STA 449F3 Jupiter apparatus to estimate the quantity of the surface hydroxyl groups. An Agilent 7900 inductively coupled plasma mass spectrometer (ICP-MS), fitted with a Micromist® concentric glass nebuliser and Peltier cooled glass spray chamber, was used to conduct the elemental analysis. The detailed description of the characterization and

the method of the uranyl adsorption analyzing are elaborated in ESI.†

3. Results and discussion

3.1. Crystal structure analyses

A sol–gel processing to fabricate the hierarchical porous crystal metal oxides with ternary composition has been proposed previously,[66] and the advantages of employing a soft chemistry method instead of a mixed oxide route and using Tyzor TE as Ti precursor rather than traditional titanium alkoxides are elucidated. Even though the compositions of the gelling material cannot be defined due to the excessive complications of the reactants (the existence of many Ce and Ti species at high pH, temperature and concentrations) along with dual templates, calcination at 800 °C leads to the formation of the metal oxides. Heating temperature is critical for crystallinity of the metal oxides. The brannerite evolution as a function of calcination temperature in absence of colloidal silica is investigated. Fig. 1 shows the XRD patterns of the $CeTi_{2.05}O_6$ composition powders calcined for 6 h from 600 to 1250 °C. Almost phase pure $CeTi_{2.05}O_6$ brannerite is formed at 600–1050 °C with small amount of CeO_2 ($2\theta \sim 28.5°$). Besides the main brannerite phase, other phases including CeO_2 (JCPDS card No. 00-001-0800, space group $Fd\bar{3}m$) and rutile-type TiO_2 ($2\theta \sim 27.5°$) (JCPDS card No. 01-089-4920, space group $P4_2/mnm$) are observed at 1150 °C. Calcination at 1250 °C results in the decrease of the peak intensity suggesting a distortion (atom rearrangement) of the brannerite structure. This structure distortion starting from ~ 1150 °C and following material decomposition at ~1250 °C have been discussed previously[19] and are mainly due to the thermodynamic stabilities of the brannerite at different temperatures. Calcination at 800 °C for 6 h is selected in all following studies. The presence of CeO_2 in all samples implies that the brannerite main phase requires Ce to be deficient as previously reported,[20,21] even though $CeTi_{2.05}O_6$ composition is used. As a result, more Ti is needed to minimize or eliminate the CeO_2 phase. Fig. S1 (ESI†) displays XRD patterns of brannerite powders calcined at 800 °C for 6 h at various Ti to Ce molar ratios with silica to brannerite being 1 : 2 (w/w). The results show the CeO_2 phase is gradually decreased with increase of Ti to Ce molar ratio from 2.05 to 2.15. At Ti to Ce molar ratio being 2.20 and 2.25, no CeO_2 phase is observed, so $CeTi_{2.2}O_6$ composition is used for further studies.

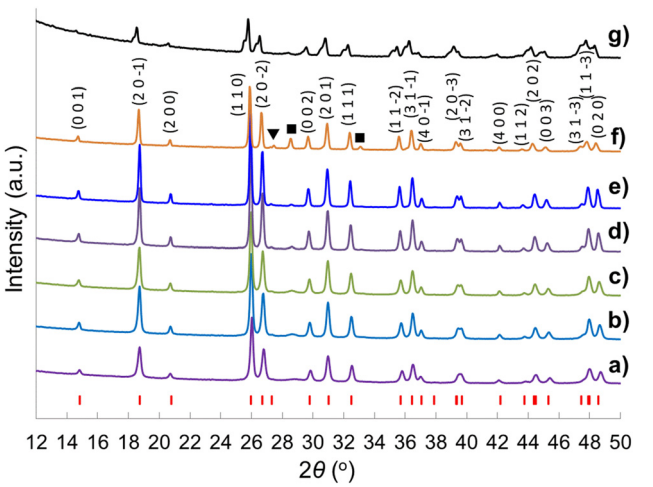

Fig. 1 XRD patterns of ($CeTi_{2.05}$)-complex powders calcined for 6 h at (a) 600 °C, (b) 700 °C, (c) 800 °C, (d) 900 °C, (e) 1050 °C, (f) 1150 °C, (g) 1250 °C. The red vertical markers beneath the brannerite patterns show the peak positions expected in the crystal structure. (▼) rutile-type TiO_2, (■) CeO_2.

$CeTi_2O_6$ brannerite has a monoclinic crystal structure with space group $C2/m$, comprising planes of anatase-like corner and edge sharing TiO_6 octahedra which form layers in the ab plane. These layers are linked along the c-axis by CeO_6 octahedra (Fig. S2, ESI†). It has been determined that Ce-brannerite is O deficient.[20–22] This O-deficient material is suggested to be charge balanced by the presence of a minor concentration of Ce^{3+} or by the Ce-deficient with the Ce^{4+} oxidation state. Stennett *et al.*[21] have investigated the crystal structure of cerium brannerite, $Ce_{0.975}Ti_2O_{5.95}$, by analyzing high resolution neutron diffraction data. The presence of both Ce and O vacancies is confirmed from Rietveld analysis, defect energy calculations, and careful investigation of the phase diagram. Formation of O vacancies at the O1 site, charge compensated by Ce vacancies, relieves considerable Coulombic repulsion and hence structural strain associated with short O1–O1 contacts forming the shared edge of neighboring TiO_6 polyhedra.

Fig. 2 shows the XRD patterns of the $CeTi_{2.20}O_6$ brannerite powders after leaching silica template, with various silica to brannerite weight ratios and different sized colloidal silica. Fig. S3 (ESI†) shows the XRD patterns of the brannerite powders before leaching silica. The XRD patterns are almost identical for all samples before (Fig. S3, ESI†) and after (Fig. 2a–d) leaching of hard template. The presence of the hard template leads to formation of the less intense and slightly more broad XRD peaks, suggesting less crystallinity and smaller crystallites of the brannerite after adding silica. The XRD data show that silica remains as amorphous state after 800 °C calcination and its presence has no significant effect on the crystallization of the brannerite and slight effect on crystallize sizes (Table 1). Brannerite crystallite sizes are calculated to be ~40 nm without hard template and ~30 nm for all templated samples, and leaching process has no effect on crystallite size. Adding silica produces smaller crystallites suggesting silica inhibits brannerite crystal growth. CeO_2 minor phase is observed when smaller silica (Φ = 6.8–8.5 nm) is used as template (Fig. 2e and f).

$CeTi_2O_6$ brannerite is higher in energy than its binary oxides with $\Delta H_{f\text{-}ox}{}^0 = +29.4 \pm 3.6$ kJ mol^{-1}. This material is entropy stabilized with $\Delta S_{f\text{-}ox}{}^0 = +18.1 \pm 2.2$ J mol^{-1} K^{-1}.[67] At 298.15 K the standard molar heat capacities is 172.78 ± 0.17 J K^{-1} mol^{-1}.[68] The free energy of formation from the oxides at 298.15 K is +15.88 ± 0.03 kJ mol^{-1}.[68] As a result, high temperature calcination, over 1351 °C ($T \geq \Delta H_{f\text{-}ox}{}^0/\Delta S_{f\text{-}ox}{}^0$), is generally required to form thermodynamically stable $CeTi_2O_6$ brannerite from the individual binary oxides *via* mixed oxide route.[17–22] In this study, Ce-brannerite is formed ≥600 °C *via* sol–gel processing with crystallite size ~30–40 nm after calcination at 800 °C. The formation of

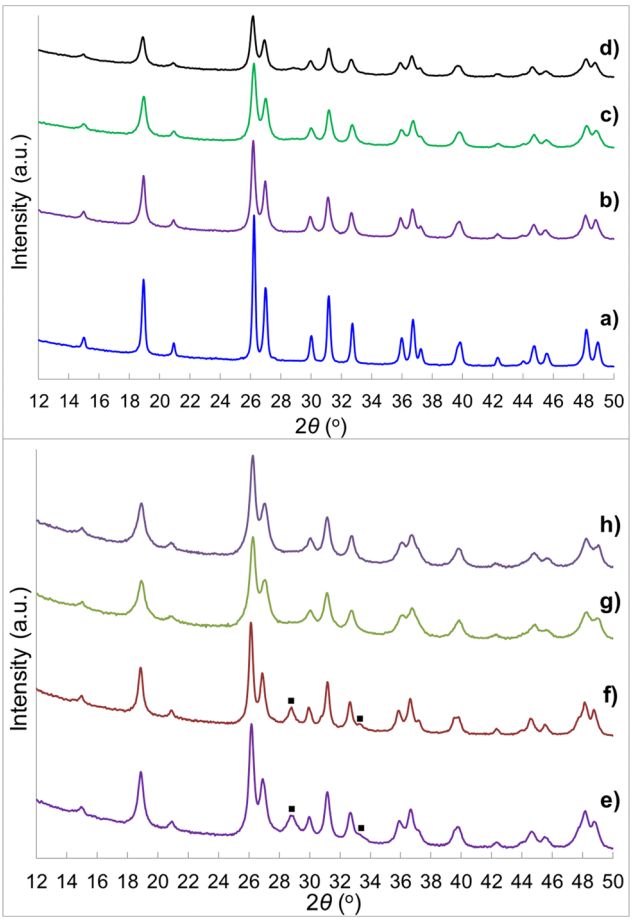

Fig. 2 XRD patterns of samples (a) w0, (b) Φ12w1–4, (c) Φ12w1–2, (d) Φ12w3–4, (e) Φ8w1–2, (f) Φ8w3–4, (g) Φ20w1–2, (h) Φ20w3–4, (■) CeO_2. Sample details are shown in Tables 2 and 3.

Table 1 Brannerite crystallite sizes (nm) calculated by Scherrer formula for (110) diffraction peak at various sizes of hard templates (Φ)

$SiO_2/CeTi_{2.20}O_6$ weight ratio	0	1 : 4	1 : 2	3 : 4
Before leaching (Φ = 12.4 nm)	41.4	33.2	33.2	33.2
After leaching (Φ = 12.4 nm)	41.4	33.2	33.2	33.2
After leaching (Φ = 6.8–8.5 nm)			27.6	33.2
After leaching (Φ = 20.3 nm)			27.6	33.2

the stable Ce-brannerite powder could be due to the "critical crystallite size" effect, *e.g.*, the tetragonal zirconia (t-ZrO_2) is usually stable between 1175 and 2370 °C, but it is metastable at room temperature when its crystallite size is <30 nm.[69,70] Large specific surface area and appreciable excess surface/interfacial free energy is to stabilize the small t-ZrO_2 grains.[70] These large surfaces are often found to be highly dynamic, which readily rearrange or react, so that energy can be reduced by processes such as adsorption. In addition, nanocrystalline ceramics (<100 nm) are expected to exhibit enhanced radiation resistance to amorphization as compared to bulk counterparts due to increased interfacial areas in the form of grain boundaries.[71] This has been confirmed by titanate pyrochlores with crystallite sizes

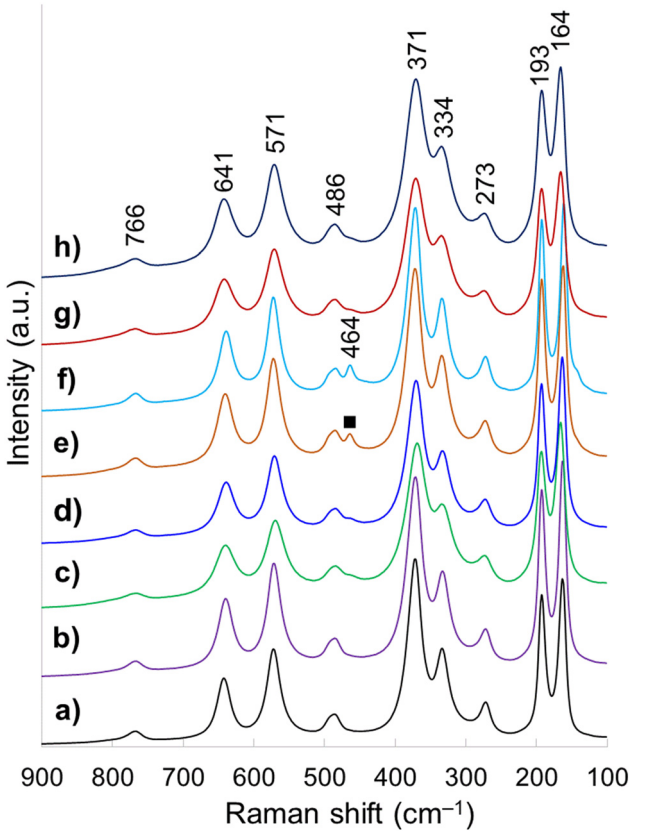

Fig. 3 Raman spectra of samples (a) w0, (b) Φ12w1–4, (c) Φ12w1–2, (d) Φ12w3–4, (e) Φ8w1–2, (f) Φ8w3–4, (g) Φ20w1–2, (h) Φ20w3–4, (■) CeO_2.

~20–30 nm.[72–74] Radiation damage has been studied for brannerite-type materials,[75–77] however, more radiation damage analyses are needed for brannerite with smaller crystalline sizes.

Raman spectroscopy is highly sensitive to short range environment of oxygen around the metal cations, *i.e.*, the coordination geometry and oxidation states. So it is able to show the vibrational modes of various MO_6 octahedral units comprising the lattice. Factor group analysis for Ce-brannerite predicts a total of $3N = 8A_g + 4B_g + 5A_u + 10B_u$ Brillouin zone center modes (N denotes the number of atoms in the molecule), in which the A_g and B_g modes are Raman active.[20,78] Raman spectra of eight template leached brannerite ($CeTi_{2.20}O_6$) powders calcined at 800 °C for 6 h (Fig. 3) at various template sizes and silica to brannerite weight ratios are nearly identical. Out of twelve theoretically predicted Raman modes, nine active modes are detected. Very strong peaks at 164 and 193 cm^{-1} are attributed to the lattice external modes. Two weak peaks at 273 and 334 cm^{-1} (A_g mode) and one very strong peak at 371 cm^{-1} (B_g mode) are due to a combination of deformation vibrations of the Ti–O–Ti units and stretching modes of CeO_6 octahedra. The 486 cm^{-1} weak band (A_g mode) is due to the symmetric stretching while the 766 cm^{-1} weak band (B_g mode) is assigned to the asymmetric stretching vibration of the Ti–O–Ti units. Strong band at 571 cm^{-1} and medium intensity band at 641 cm^{-1} (B_g mode) are generated by the edge-sharing between pairs of octahedra.[19,20,78] In addition, a weak peak observed at 464 cm^{-1} for samples using smallest

template belongs to CeO_2 possessing fluorite crystal structure (space group $Fd\bar{3}m$). All these Raman observations are in good agreement with the XRD results suggesting local structure of a small domain specimen is consistent with the average structure of the bulk material and the brannerite powder is highly homogeneous.

3.2 Powder morphology analyses

The SEM imaging (Fig. 4) is used to observe the morphology of the sub-macroscopic particulates, which are irregular shaped with size range between a few to tens of microns. These particulates are aggregation of the nanocrystals due to the introduction of the glucose as a dispersant agent. There are no significant differences for particulate size of the powders with different silica to brannerite weight ratios or different colloidal silica sizes. Further studies are needed to understand the effect of the quantity and type of the soft template/dispersant agent on the size and size distribution of the particulates. Close observation of the particulates (Fig. S4, ESI†) shows the product displays an interconnected porous network with a sponge-like structure. The size of the 'building blocks' (brannerite nanoparticles) is observed by TEM imaging.

The textural microstructure and the crystallinity of the porous brannerite after removing template are investigated using TEM. Fig. 5 and Fig. S5 (ESI†) show bright field TEM images of six brannerite samples. The microstructure of Φ12w1–4 looks like an iron sponge porous structure (Fig. 5b and Fig. S6, ESI†) because of small silica to brannerite ratio (0.57 : 1 v/v). This sponge-like crystalline microstructure has been reported for porous binary metal oxides.[79] When more silica is introduced and the amount of the brannerite component remains constant, there is not enough brannerite composition to cover the entire silica, thus brannerite particles are formed in the void spaces between the silica particles (Fig. S5, ESI†). These crystalline beads are ~15–25 nm and slightly smaller than the XRD estimation. The crystalline particles are fairly uniform suggesting the high homogeneity of the system during the synthesis. In contrast, for the sample without introducing colloidal silica (Fig. 5a), the brannerite particles are highly agglomerated, and the crystal size is ~ 50–100 nm, much larger than those of other samples. The structure of the brannerite crystals is analyzed by the selected area electron diffraction (SAED) patterns. Fig. 5d and e show strong diffractions of the SAED patterns of the brannerite crystals in either [1 3 1] or [1 1 2] zone axis from sample w0 or Φ12w1–4. The sharp dots reflect the high degree of the crystallinity of the brannerite structure at 800 °C calcination. Fig. 5f shows high resolution transmission electron microscopy (HRTEM) image from sample Φ12w1–2 in [1 5 −2] zone axis. These observations indicate that the samples possess a reasonable high crystallographic order at the atomic scale in agreement with XRD data, even though it is subjected to a low calcination temperature and short reaction time. The *d*-spacing for (2 0 1) plane is estimated to be 0.29 nm from the HRTEM image, closing to the XRD measurement, *i.e.*, 0.2883 nm (2θ = 31.02°). All TEM analyses confirm the formation of the brannerite structure under the selected synthesis conditions.

Porosity features including specific surface area, pore volume and pore diameter of the template leached brannerite powders are analyzed by nitrogen adsorption technique. The Brunauer–Emmett–Teller (BET) and non-local density functional theory (DFT) methods are used to interpret sorption isotherms. The nitrogen sorption isotherms are displayed in Fig. 6 and Fig. S7 (ESI†) while the pore size distribution and cumulate pore volume are presented in Fig. S8 and S9 (ESI†). All nitrogen sorption diagrams display the characteristics of the Type IV isotherm[80] featuring a hysteresis loop associated with the mesopores (2–50 nm). The BET results are shown in Tables 2 and 3 while the DFT data are displayed in Tables S4 and S5 (ESI†).

For sample w0 (without introducing silica but undergoing leaching process), the BET surface area and pore volume are very low at ~10 m^2 g^{-1} and ~0.08 cm^3 g^{-1}. Average pore diameter is calculated at ~31 nm and these pores are primarily due to the presence of the soft template/dispersant agent which prevents the particles from heavy agglomeration during heating. When 12.4 nm colloidal silica is used as hard template and the silica to brannerite weight ratio increases from 1 : 4 to 3 : 4, the BET surface area, pore volume and average pore diameter

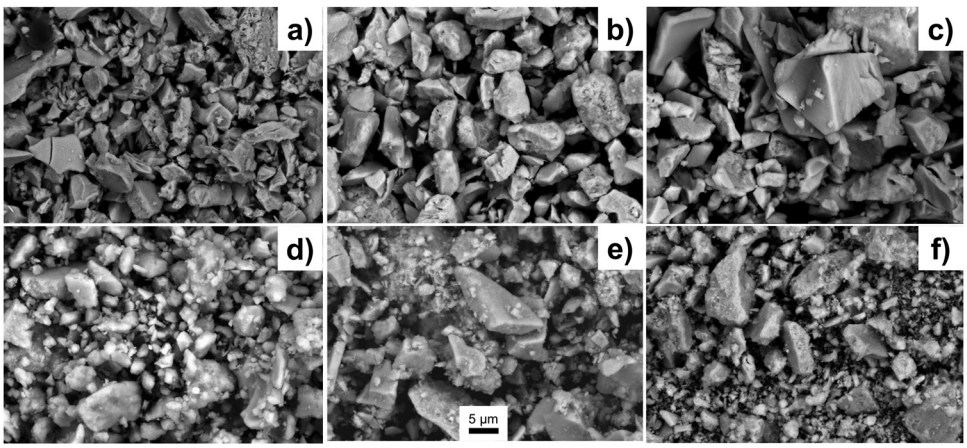

Fig. 4 SEM images of samples (a) w0, (b) Φ12w1–4, (c) Φ12w1–2, (d) Φ12w3–4, (e) Φ8w1–2, (f) Φ20w1–2.

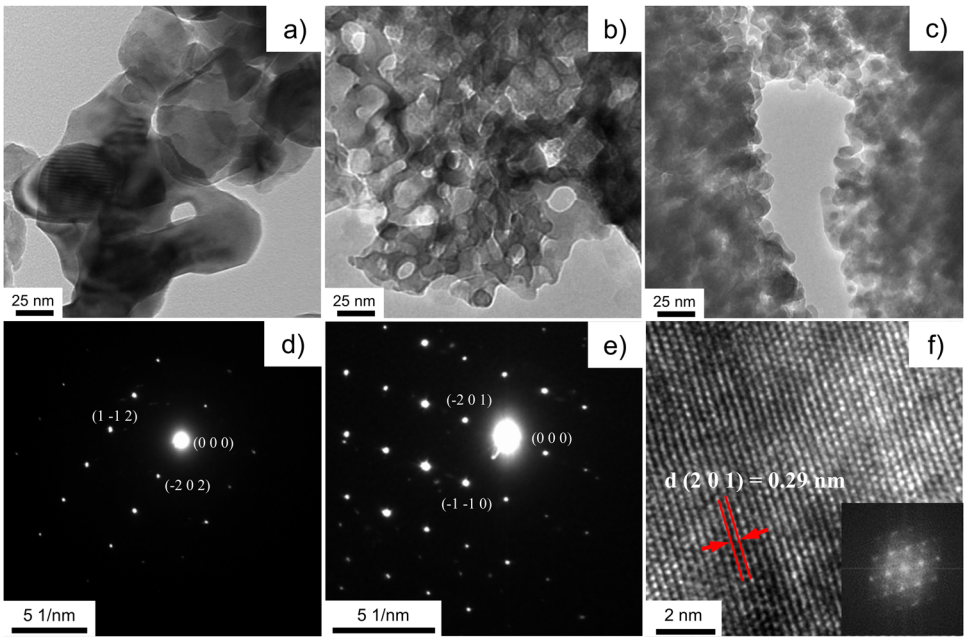

Fig. 5 Bright field TEM images of samples (a) w0, (b) Φ12w1–4, (c) Φ12w1–2, (d) SAED pattern [1 3 1] zone axis for sample w0, (e) SAED pattern [1 1 2] zone axis for sample Φ12w1–4, (f) HRTEM image for sample Φ12w1–2 in zone axis of [1 5 -2] and inserted FFT image.

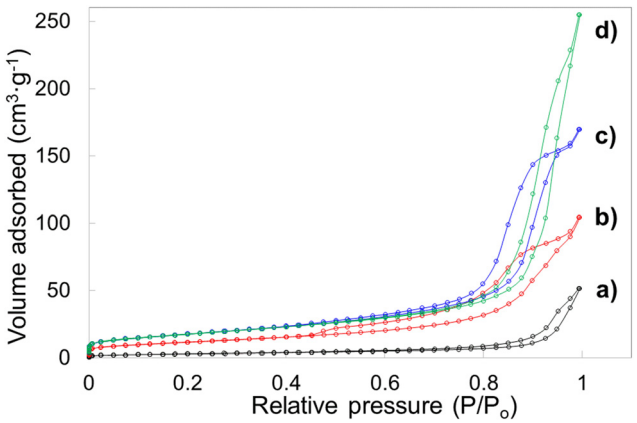

Fig. 6 Nitrogen sorption isotherms for samples (a) w0, (b) Φ12w1–4, (c) Φ12w1–2, (d) Φ12w3–4.

Table 2 BET pore structure data and surface hydroxyl group analyzing of template leached brannerite powders using 12.4 nm (Φ) colloidal silica at different silica to brannerite weight ratios

Sample	w0	Φ12w1–4	Φ12w1–2	Φ12w3–4
Silica to brannerite wt ratio	0	1 : 4	1 : 2	3 : 4
Silica to brannerite mol. ratio	0	1.38 : 1	2.76 : 1	4.14 : 1
Silica to brannerite vol. ratio	0	0.57 : 1	1.13 : 1	1.70 : 1
BET surface area ($m^2\ g^{-1}$)	10.3	42.2	63.3	64.3
BET pore volume ($cm^3\ g^{-1}$)[a]	0.080	0.162	0.262	0.394
Average pore diameter (nm)[b]	30.9	15.3	16.3	24.9
D_{OH} (OH nm^{-2})[c]	4.82	6.10	5.04	5.61
OH ($\times 10^{20}\ g^{-1}$)[d]	0.50	2.57	3.24	3.55
OH (mmol g^{-1})[e]	0.082	0.427	0.538	0.589

[a] Single-point total volume of pores at $P/P_0 > 0.99$. [b] Average pore diameter determined by BET (4V/A). [c] OH density (D_{OH}). [d] OH content ($\times 10^{20}\ g^{-1}$). [e] OH content (mmol g^{-1}) were calculated from TGA analysis. wt: weight; mol.: mole; vol.: volume.

increase from ~42 $m^2\ g^{-1}$, 0.16 $cm^3\ g^{-1}$, 15 nm to ~64 $m^2\ g^{-1}$, 0.39 $cm^3\ g^{-1}$, 25 nm, respectively. The DFT data follow the same trend with slightly different values. In addition, no pores with size <5 nm are observed, 93–98 vol% of pores are in the size range of 5–50 nm. The porosity in these samples is largely derived from intergranular voids after leaching silica templates. The addition of the hard templates not only creates vacancies in the powder after their removal, but also inhibits the growth of the brannerite grains. It is expected that increasing the amount of hard template will lead to higher intergranular volumes and smaller ceramic grains thus resulting in higher surface areas. However, this is more apparent for silica to brannerite weight ratio increment from 1 : 4 to 1 : 2, but less obvious from 1 : 2 to 3 : 4.

Table 3 BET pore structure data and surface hydroxyl group analyzing of template leached brannerite powders using different colloidal silica (Φ) at different silica to brannerite weight ratios[a]

Sample	Φ8w1–2	Φ8w3–4	Φ20w1–2	Φ20w3–4
SiO_2 (nm)	6.8–8.5	6.8–8.5	20.3	20.3
Silica to brannerite wt ratio	1 : 2	3 : 4	1 : 2	3 : 4
BET surface area ($m^2\ g^{-1}$)	76.5	55.1	99.6	97.2
BET pore volume ($cm^3\ g^{-1}$)	0.221	0.253	0.257	0.451
Average pore diameter (nm)	11.5	18.3	10.3	18.6
D_{OH} (OH nm^{-2})	4.78	5.90	5.62	5.75
OH ($\times 10^{20}\ g^{-1}$)	3.66	3.25	5.60	5.59
OH (mmol g^{-1})	0.607	0.540	0.929	0.929

[a] All denotations are the same as in Table 2.

The porosity data using the other two types of colloidal silica are displayed in Table 3. When 20.3 nm colloidal silica is used, the BET surface area approaches to 100 $m^2\ g^{-1}$ and the average pore size is ~10–18 nm. One notable result, when larger size templates are used, is the development of pores peaked ~4.8 nm after leaching silica. The DFT modelling indicates up to 16% pore volume is created by pores under 5 nm size. Compared with smaller template, larger template possesses small exposure curvature and this geometric factor may promote the chemical reaction rate on template surface.[81] As a result, these small pores are more likely derived from the spaces between brannerite crystals, rather than the cavities occupied by hard templates.

For comparison, nitrogen adsorption analyses are also carried out for powders prior to leaching 12.4 nm templates, with sorption isotherms and pore size distribution shown in Fig. S10 (ESI†) and the porosity data displayed in Table S6 (ESI†). The nitrogen isotherms display Type IV features and BET surface area is reasonably low ~2.7–13 $m^2\ g^{-1}$ with pore volume <0.04 $cm^3\ g^{-1}$, for all samples in the presence of the hard templates.

Caution is needed to interpret this type of inter-particular irregular shaped pores formed after leaching hard template since some colloidal silica might undergo dissolving and coalescing at elevated pH during drying the gelling mixture. Even though the cylindrical pore shape, which is considered for pore size calculation by DFT model, does not exactly match the voids remained after leaching silica, the pore size values should be in the same order of magnitude.[82] In addition, the results are similar when either spherical or slit pore type is selected for DFT modelling.

The pore size distribution profiles demonstrate either broader pore size distribution or multimodal porous network, for better facilitating the adsorption. Pore size distribution directly influences the adsorption kinetics, that is, the ability of the probe molecules enabling to freely access the internal

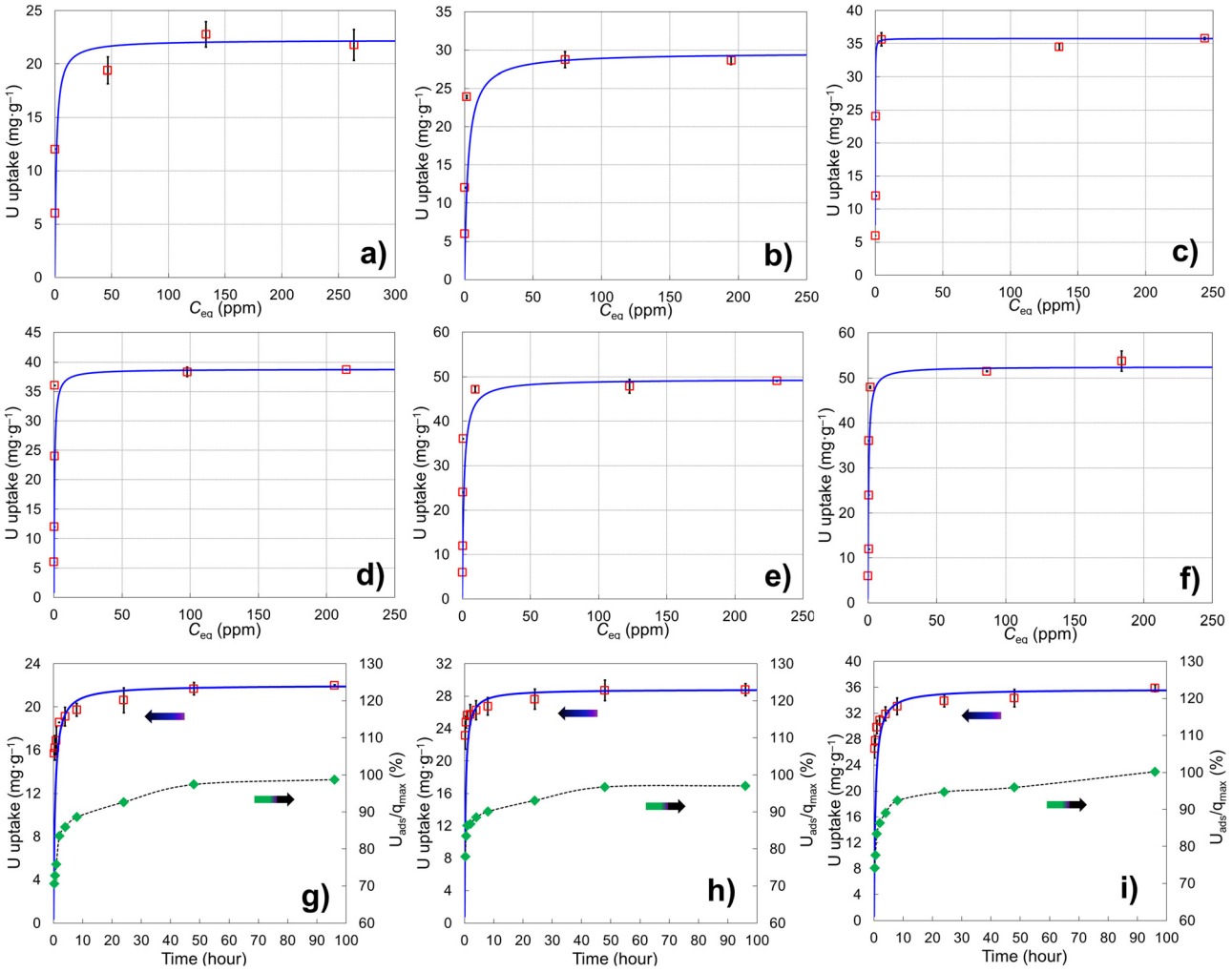

Fig. 7 (a–f) Uranium uptake adsorption isotherms and (g–i) kinetics for samples (a and g) Φ12w1–4, (b and h) Φ12w1–2, (c and i) Φ12w3–4, (d) Φ8w1–2, (e) Φ20w1–2, (f) Φ20w3–4. Blue bold lines represent Langmuir fits for isotherms and pseudo-second-order fits for kinetics with initial *U* concentration 400 mg L^{-1}. pH = 3.8, *V*/*m* = 100 mL g^{-1}. The experimental data points are expressed as (average ± 3σ, *N* = 2) and where not visible are smaller than the markers.

surface of the adsorbent particulates. This molecular accessibility is highly dependent on the pore size, especially the proportion of larger pores. The hydroxyl groups on the particle surface facilitate the affiliation between the adsorbent and the adsorbate. The surface hydroxyl group density (OH nm^{-2}) and OH content (OH g^{-1}) are estimated by TGA based on the mass loss during the heating and the results are displayed in Tables 2 and 3. Powder prepared without adding hard template has the lowest OH content, ~0.08 mmol g^{-1}. For porous brannerite powders using 12.4 nm (Φ) template, the OH content increases from ~0.43 to 0.59 mmol g^{-1} with increasing silica to brannerite weight ratio from 1 : 4 to 3 : 4. Using 20.3 nm colloidal silica as template results in materials with highest OH content, ~0.93 mmol g^{-1}, due to the higher specific surface area (~100 m^2 g^{-1}).

3.3. Uranyl adsorption analyses

Six porous brannerite powders (Table S1, ESI†) with different porosity features are used for uranyl adsorption analyses at pH 3.8 nitric acid solution, at which the UO_2^{2+} is the dominant uranium ionic species. The adsorption capacity is assessed by adsorbing UO_2^{2+} with the U initial concentration in the range of 50–700 mg L^{-1} and a solution volume to adsorbate mass ratio being 100 mL g^{-1}. The uptake adsorption isotherms are shown in Fig. 7a–f and the corresponding constants for the Langmuir model are listed in Table 4. All Langmuir profiles represent strong binding interaction between uranyl and brannerite surfaces as described by the fast uptake at initial U concentrations. The adsorption behaviors are closely complied with the Langmuir fitting, suggesting a monolayer coverage mechanism. The adsorption monolayer capacities (q_{max}) are in the range of ~0.094–0.221 mmol g^{-1} (22 to 53 mg g^{-1}) of U, and there exists a linear relation between q_{max} and the specific surface area of the porous powders (Fig. 8A). In addition, sample Φ12w3–4 reveals an outstanding b value (~ 27 in Table 4), which is an indicator for the affinity degree between adsorbent and adsorbate. This is probably due to the fact that this sample not only has larger pore diameter and pore volume, but also contains relatively higher numbers of hydroxyl groups per gram of powder.

The studies of the uranyl adsorption on porous ternary metal oxide surfaces are very limited and those using crystal porous ternary oxides are even scarcer. The porous zirconium titanium oxide mixtures are reported to undertake uranyl adsorption.[57–59] However, the products are either in amorphous state or polycrystal mixtures, with the monolayer full adsorption capacity (q_{max}) reaching up to 0.170 mmol g^{-1} under 52 m^2 g^{-1} surface area.[57] Commercially available iron embedded Fe-MnO_2 nanoporous composite has a surface area of 330 m^2 g^{-1} with uptake capacity as 0.169 mmol g^{-1}, and the surface area of the synthesized 8 nm Mn-doped iron oxides magnetic nanoparticles is 280 m^2 g^{-1} with q_{max} being 0.153 mmol g^{-1}.[51] Mesoporous porous $Y_2Ti_2O_7$ with pyrochlore structure has been formed under calcination at 900 °C with specific surface area up to 70 m^2 g^{-1} and uranyl adsorption reaching 0.249 mmol g^{-1}.[66] Even though porous $Y_2Ti_2O_7$ pyrochlore has slightly higher adsorption capacity than that of this brannerite, the latter provides alternative choice with different chemical composition and crystal structure, and higher specific surface area. It is apparent that the monolayer saturation adsorption capacity (q_{max}) has direct relationship with the specific surface area (Fig. 8A), but the 'active surface area', which the adsorbate is able to access, is more critical for effective adsorption. This 'active surface area' will be covered by the adsorbate, and may be only partial of the total specific

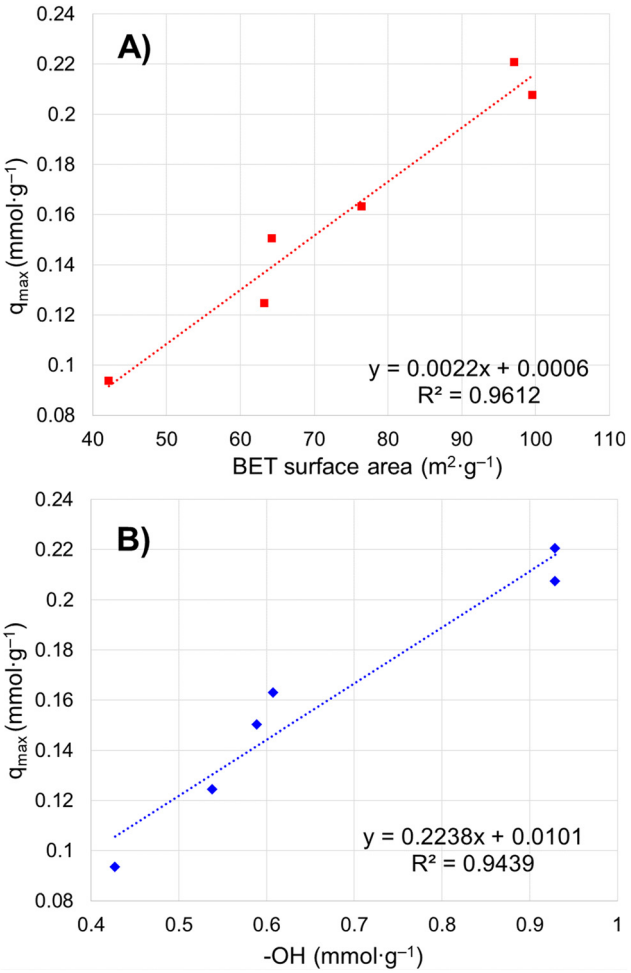

Fig. 8 Relation between maximum uranium adsorption capacity and (A) particulate specific surface area by BET modelling; (B) –OH concentration on particle surface.

Table 4 Langmuir constants for uranyl sorption capacity studies

Sample	SiO_2[a] (nm)	Ratio[b]	q_{max} (mg g^{-1})	q_{max} (mmol g^{-1})	q_{max} (μmol m^2)	b	R^2
Φ12w1–4	12.4	1 : 4	22.25	0.0935	2.314	0.7663	0.9986
Φ12w1–2	12.4	1 : 2	29.65	0.1246	1.984	0.3905	0.9982
Φ12w3–4	12.4	3 : 4	35.77	0.1503	2.472	27.28	0.9992
Φ8w1–2	6.8–8.5	1 : 2	38.80	0.1630	2.277	2.192	1.000
Φ20w1–2	20.3	1 : 2	49.45	0.2077	2.210	0.8002	0.9996
Φ20w3–4	20.3	3 : 4	52.51	0.2206	2.204	1.8764	0.9999

[a] Template diameter. [b] Template to brannerite weight ratio.

surface area and directly related with the pore size and its distribution, as well as the pore volume. Surface area contributed by micropores, if there are any, may not be covered by the adsorbate due to the accessibility issue. Furthermore, other factors such as the crystallinity and the composition of the materials exert essential roles as well for adsorption.[57]

The adsorption rates of UO_2^{2+} on three brannerites powders are investigated using C_i (initial U concentration) 400 mg L^{-1} (Table S2, ESI†). The kinetic behaviors along with the percentage of adsorbed U with regard to the q_{max} are shown in Fig. 7g–i and the corresponding pseudo-second-order kinetic results are displayed in Table 5. The equilibrium sorption capacities (q_e) are very close to the monolayer capacities (q_{max}) determined at capacity studies by Langmuir model. After soaking the powder for 15 min, adsorbed uranyl (U_{ads}) reaches ~71, 78, and 74% of the it full capacity (q_{max}), for sample Φ12w1–4, Φ12w1–2, and Φ12w3–4, respectively. At 24 h, the U_{ads}/q_{max} increases to ~93, 93, and 95% for corresponding samples. The adsorption rate closely follows the pseudo-second-order kinetic trend and over 93% of surfaces are covered by uranyl after 24 h immersion. The sample Φ12w1–2 shows slightly quicker of initial U uptake which is further demonstrated by k_2 (the overall pseudo-second-order rate constant) and h_0 (the initial adsorption rate). This could be because that the sample possesses highest proportion of mesopore volume fraction (Table 2), thus providing better pathways for UO_2^{2+} access to adsorption sites. In contrast, Φ12w1–4 shows a lower h_0 likely due to the high proportion of the smaller pores as well as smaller pore volume, thus limiting the free accessibility of the adsorbates.

Free uranyl cations are the predominant species observed in pH < 5 acidic solution. In contrast, uranyl ions form a series of polynuclear uranium species present in varying proportions in solutions with pH ≥ 5.[27] At pH 3.8, the UO_2^{2+} is the dominant species[27,57–59] which demonstrates relatively simple uranyl adsorption mechanism in respect of the adsorbate features. At this pH, uranyl ions form aquocomplexes, with $UO_2(H_2O)_5^{2+}$ identified as the most stable complex and the size of the hydrated molecular being ~ 1 nm in diameter.[83] Owing to the high proportion of the mesopores (> ~85 vol%) in the size range of 5–50 nm (Tables 2 and 3), it is reasonable to claim the diffusion rate of the complex ions is quite high, which is evidenced by the kinetics studies discussed previously. Considering the hydrogen bonded and physical adsorbed water molecule on oxide surface in an aqueous solution, porous material with micropores with size <2 nm would limit access to hydrated UO_2^{2+}. Extremely limited micropores (<2 nm) are observed by nitrogen sorption analyses for all samples synthesized using this dual template method shown in pore size distribution figures. In addition, the porous particulates with size being about a few microns observed by SEM are supposed to have shorter diffusion path distances and thus higher cation sorption rates than those of the porous monolithic type of materials. The hierarchical mesoporous structure and high porosity improve diffusion efficiency. Hydroxyl groups on particle surface may act as adsorption sites to bind uranyl ions. This action groups in either $-O^-$ or –OH state depending on solution pH play an essential role for the adsorption process. For eight samples analyzed, the average OH surface density (D_{OH}) is 5.45 ± 0.51 (average ± σ, N = 8) OH nm^{-2}, indicating ~5–6 hydroxyl species occupy one square nm on particle surface. This result is consistent with the literature data (D_{OH} = 5.4 OH nm^{-2}) for the sol–gel-made titania powders using water to titanium alkoxide precursor molar ratio being 1000 and dried at 150 °C for 24 h.[84] It is reasonable that powders possessing high surface areas (m^2 g^{-1}) normally have high OH concentration (mmol g^{-1}) (Tables 2 and 3), thus higher q_{max} (mg g^{-1}) value. A linear relationship between q_{max} and –OH concentration is shown in Fig. 8B. The samples with higher –OH concentration ~0.93 mmol g^{-1} obtain lower q_{max} than expected from the trend. One possible reason is these samples contain more smaller pores (peak pore size ~4.8 nm). Even though almost all –OH groups should be measurable by TGA analysis, not all of them are reachable by uranyl due to high proportion of the smaller pores.

An inner-sphere bidentate and tridentate surface complexation mechanisms have been reported by binding uranyl on rutile surface[85,86] and on zircon ($ZrSiO_4$),[87] respectively, at pH ~ 3. In another study, the interaction between uranyl ions and montmorillonite edge sites occurs *via* both ≡AlOH and ≡SiOH surface groups and involves three distinct surface complexes.[88] The average ratio between the quantity of –OH groups (mmol g^{-1}) and uranyl maximum adsorption capacity (mmol g^{-1}) of six samples is 4.20 ± 0.33 (average ± σ, N = 6). It is reasonable to assume that an inner-sphere tetradentate surface complexation mechanism is applied for uranyl adsorption on cerium titanate brannerite surface, though further experimental evidence is required to confirm this hypothesis.

The isoelectric point (IEP) is in the pH range of 6–10 and 4.5–7.3 for CeO_2 and TiO_2, respectively, with several exceptions, but the available IEP data of the mixed oxide are scarce, let alone the porous micron-sized polycrystal ternary oxides.[89] The point of zero charge (PZC) of the crystalline ceria, titania, and cerium titanate brannerite nanoparticles have been determined to be pH = 9.0, 4.2, and 7.5, respectively.[5] As the adsorption studies are carried out at pH 3.8, which is below the PZC of the cerium titanate, the oxide surface should be

Table 5 Uranyl adsorption pseudo-second-order kinetic constants[a]

Sample	Ratio[b]	q_e (mg g^{-1})	q_e (mmol g^{-1})	k_2 (g mg^{-1} h^{-1})	h_0 (mg g^{-1} h^{-1})	R^2
Φ12w1–4	1 : 4	22.02	0.0925	0.0808	39.2	0.9998
Φ12w1–2	1 : 2	28.84	0.1212	0.1032	85.9	0.9999
Φ12w3–4	3 : 4	35.72	0.1501	0.0533	68.0	0.9995

[a] Template size = 12.4 nm; C_i = 400 mg L^{-1}. [b] Template to brannerite weight ratio.

positively charged. UO_2^{2+} cation is the dominant species at pH 3.8, thus uranyl adsorption occurs on a positively charged oxide surfaces despite the electrostatic repulsion. As a result, the uranyl adsorption mechanism cannot be interpreted by electrostatic attraction based on the surface charge of the oxide, but an inner-sphere surface complexation.

Chemical stability tests are performed for three samples in 0.01–2 mol L^{-1} HNO_3 solutions, with V/m = 100 mL g^{-1} and 48 h contact time at room temperature. The data (Table S3, ESI†) show that the maximum amount of Ce and Ti released is <0.65 wt% of the product. Trace amount of Na (max. 0.88 wt%) and Si (max. 0.38 wt%) in powders are detected suggesting Na and Si are not completely removed during washing and leaching procedures, but the remaining quantity is negligible. All powders keeping their original crystal structure (Fig. S11, ESI†) demonstrate the phase stability both in acidic media (chemical stability tests up to 2 mol L^{-1}) and in basic solution (leaching processing at 2.5 mol L^{-1}).

Even though the method used in this study is scalable, economic, energy and time efficient for the synthesis of a crystalline porous oxide by utilizing low cost colloidal silica as template,[79] there are many unknowns for the adsorption mechanism. Many factors affect the adsorption capacity and the kinetic, and these influencing factors interact one another in many ways. In general, the 'active surface area' of the adsorbent is directly related to the sorption capacity, but this correlation cannot compare between different materials. The pore size and volume are closely linked to the sorption kinetics with larger pore volume and sizes enabling adsorbate molecules to easily access to internal surfaces, thus better facilitate the adsorption processing. The PZC/IEP and the presence of the functional groups on the material surface, along with the solution pH, are strongly related to the surface charge of the material, which affects the association between adsorbent and adsorbate, electrostatically. In addition, smaller size of the adsorbent particulate will have shorter diffusion distance for the adsorbate, whereas the dimension, shape, and the density of the adsorbate and its hydration connect with its accessibility to the internal surface of the adsorbent. Furthermore, the temperature, ion strength, volume/mass ratio and method of contacting have direct effect on the sorption capacity and kinetics. All these need to be investigated in detail. In addition, future work may also include the judicious selection the type of the templates and their quantity as well as the synthesis conditions to precisely control the porosity properties of the products. Finally various kinetic and isotherm models can be further employed[27] to interpret the data to provide additional information for better understanding the interaction mechanism between the adsorbent and the adsorbate.

4. Conclusions

Hierarchical mesoporous cerium titanate powders possessing brannerite structure have been synthesized using dual templates *via* sol–gel processing. The molar ratio of Ti and Ce being 2.20 and the calcination at 800 °C for 6 h are used to produce the brannerite with minimum secondary phases. The brannerite powders are composed of ~20–30 nm crystallized 'building blocks'. Colloidal silica with diameter ~8, 12, or 20 nm is used as the hard template, and the effect of the silica to brannerite weight ratio from 1 : 4 to 3 : 4 on material porosity is investigated. Hard template leached materials attain high specific surface area (up to ~100 m^2 g^{-1}) and pore volume (up to ~0.4 cm^3 g^{-1}), as well as the desired pore size range (5–50 nm) after degassing at 300 °C before nitrogen sorption analyzing. These 5–50 nm pores represent ~84–98% of total pore volume. The monolayer uranyl adsorption capacity (q_{max}) has linear relationship with the specific surface area of the powders with the capacity reaching ~0.221 mmol (53 mg) U per gram powder. The q_{max} and the concentration of the hydroxyl group (mmol g^{-1}) on particle surface also shows a linear relation. The materials demonstrate a surprising fast uptake rate due to the high proportion of the mesopores with adsorbed uranyl reaching over 70% of the full capacity within 15 min of contact. The employed analyzing techniques have confirmed that the synthesized brannerite powders possess high composition homogeneity, high phase and chemical stability at least in ~2 mol L^{-1} acidic and basic solutions. This porous brannerite, having unique composition, good porosity features and high physicochemical stabilities, could be applied to applications under high temperature and strong acid and base environments.

Conflicts of interest

There are no conflicts to declare.

Acknowledgements

We sincerely thank Kimbal Lu for supply of the uranyl stock solution; Ilkay Chironi for TGA data collection.

References

1 L. Yang, D. Chen, J. Zhang, Z. Lv and W. Zhang, Enhanced photocatalytic activity of porous cerium titanate using PEG4000 in sol-gel route, *Optoelectron. Adv. Mater., Rapid Commun.*, 2019, **13**, 555–559.
2 W. Zhang, Y. Tao and C. Li, Effects of PEG4000 template on sol-gel synthesis of porous cerium titanate photocatalyst, *Solid State Sci.*, 2018, **78**, 16–21.
3 W. Zhang, J. Yang and C. Li, Role of thermal treatment on sol-gel preparation of porous cerium titanate: Characterization and photocatalytic degradation of ofloxacin, *Mater. Sci. Semicond. Process.*, 2018, **85**, 33–39.
4 W. Zhang, Y. Dong, Y. Zhou, J. Li, X. Xiao and C. Li, Role of cetyltrimethyl ammonium bromide on sol–gel preparation of porous cerium titanate photocatalyst, *J. Sol-Gel Sci. Technol.*, 2018, **88**, 202–210.
5 J. Ding, Q. Zhong and S. Zhang, A new insight into catalytic ozonation with nanosized Ce–Ti oxides for NO_x removal:

Confirmation of Ce–O–Ti for active sites, *Ind. Eng. Chem. Res.*, 2015, **54**, 2012–2022.

6 A. Verma, A. Goyal and R. K. Sharma, Microstructural, photocatalysis and electrochemical investigations on $CeTi_2O_6$ thin films, *Thin Solid Films*, 2008, **516**, 4925–4933.

7 S. Otsuka-Yao-Matsuo, T. Omata and M. Yoshimura, Photocatalytic behavior of cerium titanates, $CeTiO_4$ and $CeTi_2O_6$ and their composite powders with $SrTiO_3$, *J. Alloys Compd.*, 2004, **376**, 262–267.

8 A. Verma and S. A. Agnihotry, *Sol-gel process for the preparation of nanocrystalline $CeTi_2O_6$ powder, US Pat.*, 2013/8349284 B2, 2013.

9 V. Amita, A. S. Avinash and B. A. Kumar, *Monoclinic $CeTi_2O_6$ thin film and sol-gel process for the preparation thereof, US Pat.*, 2010/7678413 B2, 2010.

10 A. Verma, A. K. Srivastava and K. N. Sood, Effect of precursor sol's aging on properties of nanostructured thin films with coexistent CeO_2 and $CeTi_2O_6$ phases, *Solid State Ionics*, 2007, **178**, 1288–1296.

11 M. Yoshida and S. Ueda, *Ternary-type complex oxide abrasive for polishing of semiconductor wafer, contains ternary-type complex oxide particles containing cerium-titanium oxide phase which has brannerite structure of monoclinic system, Jpn Pat.*, 2007116081-A, 2007.

12 M. Yoshida, N. Koyama, T. Ashizawa, Y. Sakata and H. Imamura, A new cerium-based ternary oxide slurry, $CeTi_2O_6$, for chemical-mechanical polishing, *Jpn. J. Appl. Phys.*, 2007, **46**, 977–979.

13 D. J. Bailey, M. C. Stennett, B. Ravel, D. Grolimund and N. C. Hyatt, Synthesis and characterisation of brannerite compositions $(U_{0.9}Ce_{0.1})_{1-x}M_xTi_2O_6$ (M = Gd^{3+}, Ca^{2+}) for the immobilisation of MOX residues, *RSC Adv.*, 2018, **8**, 2092–2099.

14 S. V. Stefanovsky, S. V. Yudintsev, A. A. Shiryaev, V. Y. Murzin and A. L. Trigub, Phase partitioning and uranium speciation in brannerite-based ceramics, *J. Eur. Ceram. Soc.*, 2017, **37**, 771–777.

15 R. Gilligan and A. N. Nikoloski, The extraction of uranium from brannerite – A literature review, *Miner. Eng.*, 2015, **71**, 34–48.

16 S. Shahab Naghavi, J. He and C. Wolverton, $CeTi_2O_6$ – A promising oxide for solar thermochemical hydrogen production, *ACS Appl. Mater. Interfaces*, 2020, **12**, 21521–21527.

17 M. C. Dixon Wilkins, E. R. Maddrell, M. C. Stennett and N. C. Hyatt, The effect of temperature on the stability and cerium oxidation state of $CeTi_2O_6$ in inert and oxidizing atmospheres, *Inorg. Chem.*, 2020, **59**, 17364–17373.

18 E. R. Aluri, L. M. Bachiu, A. P. Grosvenor, S. H. Forbes and J. E. Greedan, Assessing the oxidation states and structural stability of the Ce analogue of brannerite, *Surf. Interface Anal.*, 2017, **49**, 1335–1344.

19 L. Kong, D. J. Gregg, E. R. Vance, I. Karatchevtseva, G. R. Lumpkin, M. G. Blackford, R. Holmes, M. Jovanovic and G. Triani, Preparation of cerium titanate brannerite by solution combustion, and phase transformation during heat treatment, *J. Eur. Ceram. Soc.*, 2017, **37**, 2179–2187.

20 L. Kong, D. J. Gregg, I. Karatchevtseva, Z. Zhang, M. G. Blackford, S. C. Middleburgh, G. R. Lumpkin and G. Triani, Novel chemical synthesis and characterization of $CeTi_2O_6$ brannerite, *Inorg. Chem.*, 2014, **53**, 6761–6768.

21 M. C. Stennett, C. L. Freeman, A. S. Gandy and N. C. Hyatt, Crystal structure and non-stoichiometry of cerium brannerite: $Ce_{0.975}Ti_2O_{5.95}$, *J. Solid State Chem.*, 2012, **192**, 172–178.

22 L. T. Huynh, S. B. Eger, J. D. S. Walker, J. R. Hayes, M. W. Gaultois and A. P. Grosvenor, How temperature influences the stoichiometry of $CeTi_2O_6$, *Solid State Sci.*, 2012, **14**, 761–767.

23 V. Valeš, L. Matějová, Z. Matěj, T. Brunátová and V. Holý, Crystallization kinetics study of cerium titanate $CeTi_2O_6$, *J. Phys. Chem. Solids*, 2014, **75**, 265–270.

24 T. Kidchob, L. Malfatti, D. Marongiu, S. Enzo and P. Innocenzi, An alternative sol-gel route for the preparation of thin films in CeO_2-TiO_2 binary system, *Thin Solid Films*, 2010, **518**, 1653–1657.

25 T. Kidchob, L. Malfatti, D. Marongiu, S. Enzo and P. Innocenzi, Formation of cerium titanate, $CeTi_2O_6$, in sol-gel films studied by XRD and FAR infrared spectroscopy, *J. Sol-Gel Sci, Technol.*, 2009, **52**, 356–361.

26 L. Matějová, V. Valeš, R. Fajgar, Z. Matěj, V. Holý and O. Šolcová, Reverse micelles directed synthesis of TiO_2-CeO_2 mixed oxides and investigation of their crystal structure and morphology, *J. Solid State Chem.*, 2013, **198**, 485–495.

27 Y. Xie, C. Chen, X. Ren, X. Wang, H. Wang and X. Wang, Emerging natural and tailored materials for uranium-contaminated water treatment and environmental remediation, *Prog. Mater. Sci.*, 2019, **103**, 180–234.

28 H.-C. zur Loye, T. Besmann, J. Amoroso, K. Brinkman, A. Grandjean, C. H. Henager, S. Hu, S. T. Misture, S. R. Phillpot, N. B. Shustova, H. Wang, R. J. Koch, G. Morrison and E. Dolgopolova, Hierarchical materials as tailored nuclear waste forms: A perspective, *Chem. Mater.*, 2018, **30**, 4475–4488.

29 K. Vellingiri, K.-H. Kim, A. Pournara and A. Deep, Towards high-efficiency sorptive capture of radionuclides in solution and gas, *Prog. Mater. Sci.*, 2018, **94**, 1–67.

30 T. Le Nedelec, A. Charlot, F. Calard, F. Cuer, A. Leydier and A. Grandjean, Uranium adsorption from sulfuric acid media using silica materials functionalised with amide and phosphorous ligands, *New J. Chem.*, 2018, **42**, 14300.

31 E. Rosenberg, G. Pinson, R. Tsosie, H. Tutu and E. Cukrowska, Uranium remediation by ion exchange and sorption methods: A critical review, *Johnson Matthey Technol. Rev.*, 2016, **60**, 59–77.

32 M. Gao, G. Zhu and C. Gao, A review: Adsorption materials for the removal and recovery of uranium from aqueous solutions, *Energy Environ. Focus*, 2014, **3**, 219–226.

33 L. Chen, H. Xin, Y. Fang, C. Zhang, F. Zhang, X. Cao, C. Zhang and X. Li, Application of metal oxide heterostructures in arsenic removal from contaminated water, *J. Nanomater.*, 2014, **2014**, 793610.

34 P. Makowski, X. Deschanels, A. Grandjean, D. Meyer, G. Toquer and F. Goettmann, Mesoporous materials in

the field of nuclear industry: Applications and perspectives, *New J. Chem.*, 2012, **36**, 531–541.
35 R. K. Eby, R. C. Ewing and R. C. Birtcher, The amorphization of complex silicates by ion-beam irradiation, *J. Mater. Res.*, 1992, **7**, 3080–3102.
36 Y. Lou, S. Dourdain, C. Rey, Y. Serruys, D. Simeone, N. Mollard and X. Deschanels, Structure evolution of mesoporous silica under heavy ion irradiations of intermediate energies, *Microporous Mesoporous Mater.*, 2017, **251**, 146–154.
37 C. Jo, J. Hwang, W.-G. Lim, J. Lim, K. Hur and J. Lee, Multiscale phase separations for hierarchically ordered macro/sesostructured metal oxides, *Adv. Mater.*, 2018, **30**, 1703829.
38 J. Wei, Z. Sun, W. Luo, Y. Li, A. A. Elzatahry, A. M. Al-Enizi, Y. Deng and D. Zhao, New insight into the synthesis of large-pore ordered mesoporous materials, *J. Am. Chem. Soc.*, 2017, **139**, 1706–1713.
39 A. Feinle, M. S. Elsaesser and N. Hüsing, Sol–gel synthesis of monolithic materials with hierarchical porosity, *Chem. Soc. Rev.*, 2016, **45**, 3377–3399.
40 L.-B. Sun, X.-Q. Liu and H.-C. Zhou, Design and fabrication of mesoporous heterogeneous basic catalysts, *Chem. Soc. Rev.*, 2015, **44**, 5092–5147.
41 D. Gu and F. Schüth, Synthesis of non-siliceous mesoporous oxides, *Chem. Soc. Rev.*, 2014, **43**, 313–344.
42 A. Walcarius, Mesoporous materials and electrochemistry, *Chem. Soc. Rev.*, 2013, **42**, 4098–4140.
43 V. Valtchev and L. Tosheva, Porous nanosized particles: preparation, properties, and applications, *Chem. Rev.*, 2013, **113**, 6734–6760.
44 W. Li and D. Zhao, An overview of the synthesis of ordered mesoporous materials, *Chem. Commun.*, 2013, **49**, 943–946.
45 W. Li, Q. Yue, Y. Deng and D. Zhao, Ordered mesoporous materials based on interfacial assembly and engineering, *Adv. Mater.*, 2013, **25**, 5129–5152.
46 Y. Ren, Z. Ma and P. G. Bruce, Ordered mesoporous metal oxides: Synthesis and applications, *Chem. Soc. Rev.*, 2012, **41**, 4909–4927.
47 E. Broda, A. Gładysz-Płaska, E. Skwarek and V. V. Payentko, Structural properties and adsorption of uranyl ions on the nanocomposite hydroxyapatite/white clay, *Appl. Nanosci.*, 2022, **12**, 1101–1111.
48 E. Skwarek, A. Gładysz-Płaska, J. B. Choromańska and E. Broda, Adsorption of uranium ions on nano-hydroxyapatite and modified by Ca and Ag ions, *Adsorption*, 2019, **25**, 639–647.
49 E. Skwarek, A. Gładysz–Płaska and Y. Bolbukh, Adsorption of uranyl ions at the nano-hydroxyapatite and its modification, *Nanoscale Res. Lett.*, 2017, **12**, 278.
50 S. Huang, H. Pang, L. Li, S. Jiang, T. Wen, L. Zhuang, B. Hu and X. Wang, Unexpected ultrafast and high adsorption of U(VI) and Eu(III) from solution using porous Al_2O_3 microspheres derived from MIL-53, *Chem. Eng. J.*, 2018, **353**, 157–166.
51 W. Chouyyok, C. L. Warner, K. E. Mackie, M. G. Warner, G. A. Gill and R. Shane Addleman, Nanostructured metal oxide sorbents for the collection and recovery of uranium from seawater, *Ind. Eng. Chem. Res.*, 2016, **55**, 4195–4207.
52 E. Calì, J. Qi, O. Preedy, S. Chen, D. Boldrin, W. R. Branford, L. Vandeperre and M. P. Ryan, Functionalised magnetic nanoparticles for uranium adsorption with ultra-high capacity and selectivity, *J. Mater. Chem. A*, 2018, **6**, 3063–3073.
53 P. Singhal, S. K. Jha, S. P. Pandey and S. Neogy, Rapid extraction of uranium from sea water using Fe_3O_4 and humic acid coated Fe_3O_4 nanoparticles, *J. Hazard. Mater.*, 2017, **335**, 152–161.
54 M. J. O'Hara, J. C. Carter, C. L. Warner, M. G. Warner and R. Shane Addleman, Magnetic iron oxide and manganese-doped iron oxide nanoparticles for the collection of alpha-emitting radionuclides from aqueous solutions, *RSC Adv.*, 2016, **6**, 105239.
55 L. Tan, X. Zhang, Q. Liu, X. Jing, J. Liu, D. Song, S. Hu, L. Liu and J. Wang, Synthesis of Fe_3O_4@TiO_2 core–shell magnetic composites for highly efficient sorption of uranium (VI), *Colloids Surf., A*, 2015, **469**, 279–280.
56 J. Veliscek-Carolan, K. A. Jolliffe and T. L. Hanley, Selective sorption of actinides by titania nanoparticles covalently functionalized with simple organic ligands, *ACS Appl. Mater. Interfaces*, 2013, **5**, 11984–11994.
57 M. Chee Kimling, N. Scales, T. L. Hanley and R. A. Caruso, Uranyl-sorption properties of amorphous and crystalline TiO_2/ZrO_2 millimeter-sized hierarchically porous beads, *Environ. Sci. Technol.*, 2012, **46**, 7913–7920.
58 G. L. Drisko, M. Chee Kimling, N. Scales, A. Ide, E. Sizgek, R. A. Caruso and V. Luca, One-pot preparation and uranyl adsorption properties of hierarchically porous zirconium titanium oxide beads using phase separation processes to vary macropore morphology, *Langmuir*, 2010, **26**, 17581–17588.
59 G. D. Sizgek, C. S. Griffith, E. Sizgek and V. Luca, Mesoporous zirconium titanium oxides. part 3. synthesis and adsorption properties of unfunctionalized and phosphonate-functionalized hierarchical polyacrylonitrile-F-127-templated beads, *Langmuir*, 2009, **25**, 11874–11882.
60 Q. Yuan, Y. Liu, L.-L. Li, Z.-X. Li, C.-J. Fang, W.-T. Duan, X.-G. Li and C.-H. Yan, Highly ordered mesoporous titania–zirconia photocatalyst for applications in degradation of rhodamine-B and hydrogen evolution, *Microporous Mesoporous Mater.*, 2009, **124**, 169–178.
61 B. M. Reddy and A. Khan, Recent advances on TiO_2-ZrO_2 mixed oxides as catalysts and catalyst supports, *Catal. Rev.: Sci. Eng.*, 2005, **47**, 257–296.
62 S. Deng, Z. Li, J. Huang and G. Yu, Preparation, characterization and application of a Ce–Ti oxide adsorbent for enhanced removal of arsenate from water, *J. Hazard. Mater.*, 2010, **179**, 1014–1021.
63 V. Luca, W. K. Bertram, J. Widjaja, D. R. G. Mitchell, C. S. Griffith and E. Drabarek, Synthesis of mesoporous zirconium titanates using alkycarboxylate surfactants and their transformation to dense ceramics, *Microporous Mesoporous Mater.*, 2007, **103**, 123–133.
64 A. E. Ringwood, S. E. Kesson, N. G. Ware, W. Hibberson and A. Major, Immobilization of high-level nuclear-reactor wastes in synroc, *Nature*, 1979, **278**, 219–223.

65 *CRC Handbook of Chemistry and Physics*, ed. W. M. Haynes, CRC Press, Boca Raton, FL, USA, 92nd edn, 2011.
66 L. Kong, I. Karatchevtseva, T. Wei and N. Scales, Synthesis of hierarchical mesoporous $Ln_2Ti_2O_7$ pyrochlores and uranyl adsorption properties, *J. Mater. Sci. Technol.*, 2022, **113**, 22–32.
67 K. B. Helean, A. Navrotsky, G. R. Lumpkin, M. Colella, J. Lian, R. C. Ewing, B. Ebbinghaus and J. G. Catalano, Enthalpies of formation of U-, Th-, Ce-brannerite: Implications for plutonium immobilization, *J. Nucl. Mater.*, 2003, **320**, 231–244.
68 M. H. Donaldson, R. Stevens, B. E. Lang, J. Boerio-Goates, B. F. Woodfield, R. L. Putnam and A. Navrotsky, Heat capacities and absolute entropies of UTi_2O_6 and $CeTi_2O_6$, *J. Therm. Anal. Calorim.*, 2005, **81**, 617–625.
69 L. Kong, I. Karatchevtseva, H. Zhu, M. J. Qin and Z. Aly, Synthesis and microstructure characterization of tetragonal $Zr_{1-x}Ti_xO_2$ (x = 0–1) solid solutions, *J. Mater. Sci. Technol.*, 2019, **35**, 1966–1976.
70 R. C. Garvie, The occurrence of metastable tetragonal zirconia as a crystallite size effect, *J. Phys. Chem.*, 1965, **69**, 1238–1243.
71 S. Dey, J. W. Drazin, Y. Wang, J. A. Valdez, T. G. Holesinger, B. P. Uberuaga and R. H. R. Castro, Radiation tolerance of nanocrystalline ceramics: Insights from yttria stabilized zirconia, *Sci. Rep.*, 2015, **5**, 7746.
72 J. Wen, C. Sun, P. P. Dholabhai, Y. Xia, M. Tang, D. Chen, D. Y. Yang, Y. H. Li, B. P. Uberuaga and Y. Q. Wang, Temperature dependence of the radiation tolerance of nanocrystalline pyrochlores $A_2Ti_2O_7$ (A = Gd, Ho and Lu), *Acta Mater.*, 2016, **110**, 175–184.
73 J. Zhang, J. Lian, A. F. Fuentes, F. Zhang, M. Lang, F. Lu and R. C. Ewing, Enhanced radiation resistance of nanocrystalline pyrochlore $Gd_2(Ti_{0.65}Zr_{0.35})_2O_7$, *Appl. Phys. Lett.*, 2009, **94**, 243110.
74 J. Zhang, J. Lian, F. Zhang, J. Wang, A. F. Fuentes and R. C. Ewing, Intrinsic structural disorder and radiation response of nanocrystalline $Gd_2(Ti_{0.65}Zr_{0.35})_2O_7$ pyrochlore, *J. Phys. Chem. C*, 2010, **114**, 11810–11815.
75 F. X. Zhang, M. Lang, Z. Liu and R. C. Ewing, Phase stability of some actinides with brannerite structure at high pressures, *J. Solid State Chem.*, 2011, **184**, 2834–2839.
76 J. Lian, L. M. Wang, G. R. Lumpkin and R. C. Ewing, Heavy ion irradiation effects of brannerite-type ceramics, *Nucl. Instrum. Methods Phys. Res., Sect. B*, 2002, **191**, 565–570.
77 G. R. Lumpkin, K. L. Smith and M. G. Blackford, Heavy ion irradiation studies of columbite, brannerite, and pyrochlore structure types, *J. Nucl. Mater.*, 2001, **289**, 177–187.
78 E. J. Baran, C. I. Cabello and A. G. Nord, Raman spectra of some $M^{II}V_2O_6$ brannerite-type metavanadates, *J. Raman Spectrosc.*, 1987, **18**, 405–407.
79 K. U. Chan, A. Voskanyan and C. Y. V. Li, *Method of producing a porous crystalline material with a highly uniform structure, US Pat.*, 2019/0062225 A1, 2019.
80 M. Thommes, K. Kaneko, A. V. Neimark, J. P. Olivier, F. Rodriguez-Reinoso, J. Rouquerol and K. S. W. Sing, Physisorption of gases, with special reference to the evaluation of surface area and pore size distribution (IUPAC technical report), *Pure Appl. Chem.*, 2015, **87**, 1051–1069.
81 C. Eun, Effect of surface curvature on diffusion-limited reactions on a curved surface, *J. Chem. Phys.*, 2017, **147**, 184112.
82 J. V. Rocha, D. Barrera and K. Sapag, Improvement in the pore size distribution for ordered mesoporous materials with cylindrical and spherical pores using the Kelvin equation, *Top. Catal.*, 2011, **54**, 121–134.
83 Y. S. Shin, M. C. Burleigh, S. Dai, C. E. Barnes and Z. L. Xue, Investigation of uranyl adsorption on mesoporous titanium-based sorbents, *Radiochim. Acta*, 1999, **84**, 37–42.
84 S. Tsushima and A. Suzuki, Hydration numbers of pentavalent and hexavalent uranyl, neptunyl, and plutonyl, *J. Mol. Struct. THEOCHEM*, 2000, **529**, 21–25.
85 H. Perron, J. Roques, C. Domain, R. Drot, E. Simoni and H. Catalette, Theoretical investigation of the uranyl ion sorption on the rutile TiO_2(110) face, *Inorg. Chem.*, 2008, **47**, 10991–10997.
86 J. Vandenborre, R. Drot and E. Simoni, Interaction mechanisms between uranium(VI) and rutile titanium dioxide: From single crystal to powder, *Inorg. Chem.*, 2007, **46**, 1291–1296.
87 C. Lomenech, E. Simoni, R. Drot, J. J. Ehrhardt and J. Mielczarski, Sorption of uranium(VI) species on zircon: Structural investigation of the solid/solution interface, *J. Colloid Interface Sci.*, 2003, **261**, 221–232.
88 A. Kowal-Fouchard, R. Drot, E. Simoni and J. J. Ehrhardt, Use of spectroscopic techniques for uranium(VI)/montmorillonite interaction modeling, *Environ. Sci. Technol.*, 2004, **38**, 1399–1407.
89 M. Kosmulski, Isoelectric points and points of zero charge of metal (hydr)oxides: 50 years after Parks' review, *Adv. Colloid Interface Sci.*, 2016, **238**, 1–61.

